Supplement of

Inland migration of ~~Pine Island and Thwaites Glacier surface~~ near-surface crevasses in the Amundsen Sea ~~Embayment~~Sector, West Antarctica

Andrew O. Hoffman et al.

Correspondence: Andrew Hoffman (aoh2111@columbia.edu)

1 Introduction

An overview of the processing steps and convolutions used in the U-net model is shown in Supplementary Figure 1, with tables that include the parameters chosen based on model performance.

2 U-net architecture and training

5   The U-net we implemented includes 3 down-sampling layers, and 3 up-sampling layers that were trained on 1600 images from the Amundsen sea Embayment. The trained network takes preprocessed input images and produces images with pixel-wise probability that the individual pixel in question includes a crevasse. These probabilities are used to create binary detection masks using the F1-score on independent training data. The F1-score is a measure of the accuracy of binary classification algorithms and was used to diagnose the precision and recall of pixel-wise crevasse classification based on a threshold

10   probability. The F1 can be written formally as:

$$F1 = \frac{TP}{(TP + \frac{(FP+FN)}{2})} \tag{1}$$

Where TP is the number of true positives, FP is the number of false positives, and FN is the number of false negatives.

3 Plotting of principal surface stress failure envelopes

Surface observations of ice motion can be used to determine strain rates and strain-rate measurements can be converted to

15   stress using a constitutive relation. Nye (1959) outlined the method for conversion from surface strain rates to surface stress in one of the first applications of the constitutive relation for snow and ice. Here, we briefly summarize this calculation with some changes in convention following the work of (Vaughan, 1993; Bindschadler et al., 1996; Veen, 1999; Alley et al., 2018) and choose a form that is defined in terms of effective viscosity that could be used for either ice and firn.

Assuming a two-dimensional Cartesian coordinate system, the magnitudes of the principal surface strain rates are related to the directional surface strain rates by (Nye, 1959):

$$\dot{\epsilon}_{1surf} = \frac{1}{2}\left(\dot{\epsilon}_x + \dot{\epsilon}_y\right) - \sqrt{\frac{1}{4}\left(\dot{\epsilon}_x - \dot{\epsilon}_y\right)^2 + \dot{\epsilon}_{xy}^2} \tag{2}$$

$$\dot{\epsilon}_{2surf} = \frac{1}{2}\left(\dot{\epsilon}_x + \dot{\epsilon}_y\right) + \sqrt{\frac{1}{4}\left(\dot{\epsilon}_x - \dot{\epsilon}_y\right)^2 + \dot{\epsilon}_{xy}^2} \tag{3}$$

where we have assigned the first principal strain rate as the larger principal strain rate. The measured principal surface strain rates can then be used to calculate the principal surface stress magnitudes following Glen's flow law (Nye, 1959; Vaughan, 1993; Veen, 1999):

$$\sigma_{1surf} = 2\eta\dot{\epsilon}_{1surf} + \eta\dot{\epsilon}_{2surf} \tag{4}$$

$$\sigma_{2surf} = \eta\dot{\epsilon}_{1surf} + 2\eta\dot{\epsilon}_{2surf} \tag{5}$$

where $\eta = \frac{1}{2}A^{-1/n}\dot{\epsilon}_e^{-(n-1)/n}$ is the effective viscosity of the ice, $\dot{\epsilon}_e$ is the effective strain rate, and $n = 3$ is the flow law exponent. A is the temperature (and likely flow-history) dependent creep parameter; here we set $A = 5.2 \times 10^{-25}$ s^{-1} Pa^{-3}, which is appropriate for ice at a temperature of $-10°$C (Cuffey and Paterson, 2010). We also considered a number of constitutive relations for firn (Ambach and Eisner, 1986; Ambach et al., 1993, 1995; Arthern et al., 2010; Morris and Wingham, 2014). Many of these relations depend on parameters that are unknown for this study area, namely firn density, temperature-depth profiles, and viscosity parameters. We choose an empirically determined firn shear viscosity of 4.9×10^9 KPa·s from measurements of polar firn in Greenland at a temperature of $-10°$C and density of 700 kg/m^3 (Haefeli, 1967). Results for ice fluidity are shown in the text. The results assuming a firn fluidity (effective viscosity $\sim 10^9$ Pa) further reduce the inferred effective stresses presented in Figures 7, 8 and indicate that the surface may be weaker than what is reported in this study and in previous satellite crevasse observational work (i.e. Vaughan, 1993; Lai et al., 2020; Grinsted et al., 2023). The ovoid shape of the failure envelopes assuming a fluidity consistent with firn remains the same (i.e. the structure remains consistent with von Mises failure). We choose to use ice fluidity as this parameterization as it represents an upper bound on the inferred tensile strength of the near surface.

By the von Mises failure criterion, if

$$\sigma_t^2 < \sigma_{1surf}^2 + \sigma_{2surf}^2 - \sigma_{1surf}\sigma_{2surf} \tag{6}$$

then crevassing should occur, where σ_t is the tensile strength to ice. This failure criterion depends critically on the value for the tensile strength of ice, which is temperature and flow history dependent. The conversion between surface strain rates and surface stresses has a similar temperature and flow history dependence through the effective viscosity and flow law, but the temperature relationship is somewhat better established from both laboratory and field studies.

To evaluate the applicability of analytic failure theory, we create maps of the two principal surface stresses from the surface strain rates following the methods outlined above. We then plot crevasse locations as a function of surface stresses, where x-axis is the first principal stress and the y-axis is the second principal stress (Fig. 7a). In this basis space, the tensile strength corresponding to the von Mises failure criterion should appear as an ovaloid curve that demarks crevassed pixels from un-crevassed pixels. We create crevasse failure maps for each quarter of data from 2015 to 2022 for Thwaites Glacier and plot the crevasse locations in the surface stress basis space (Fig. 7a). The prominent ovaloid structure defines a clear relationship between stress and (we have not assumed this form) is broadly consistent with expectations from the von Mises criterion. The spread of values, however, suggests that assuming a single critical tensile strength is not appropriate.
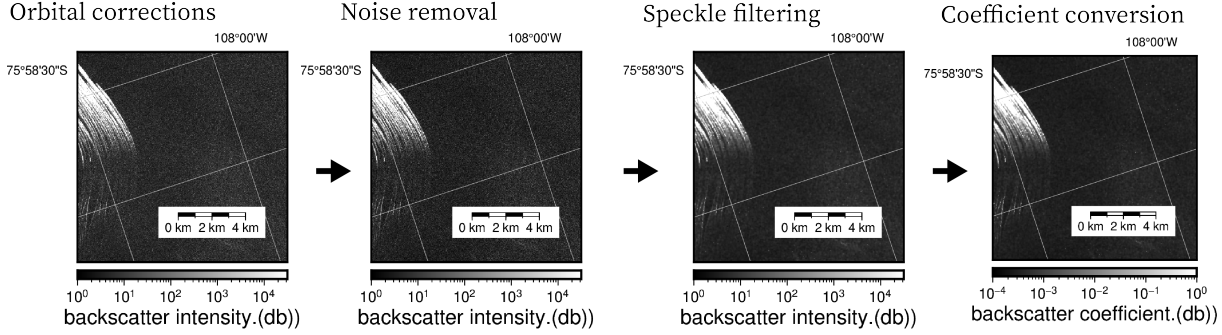

Figure S1. Preprocessing steps that precede U-net training and crevasse segmentation from SAR imagery. These steps transform the backscatter intensity and after correcting for thermal and instrument noise we convert the backscatter intensity into a backscatter coefficient.
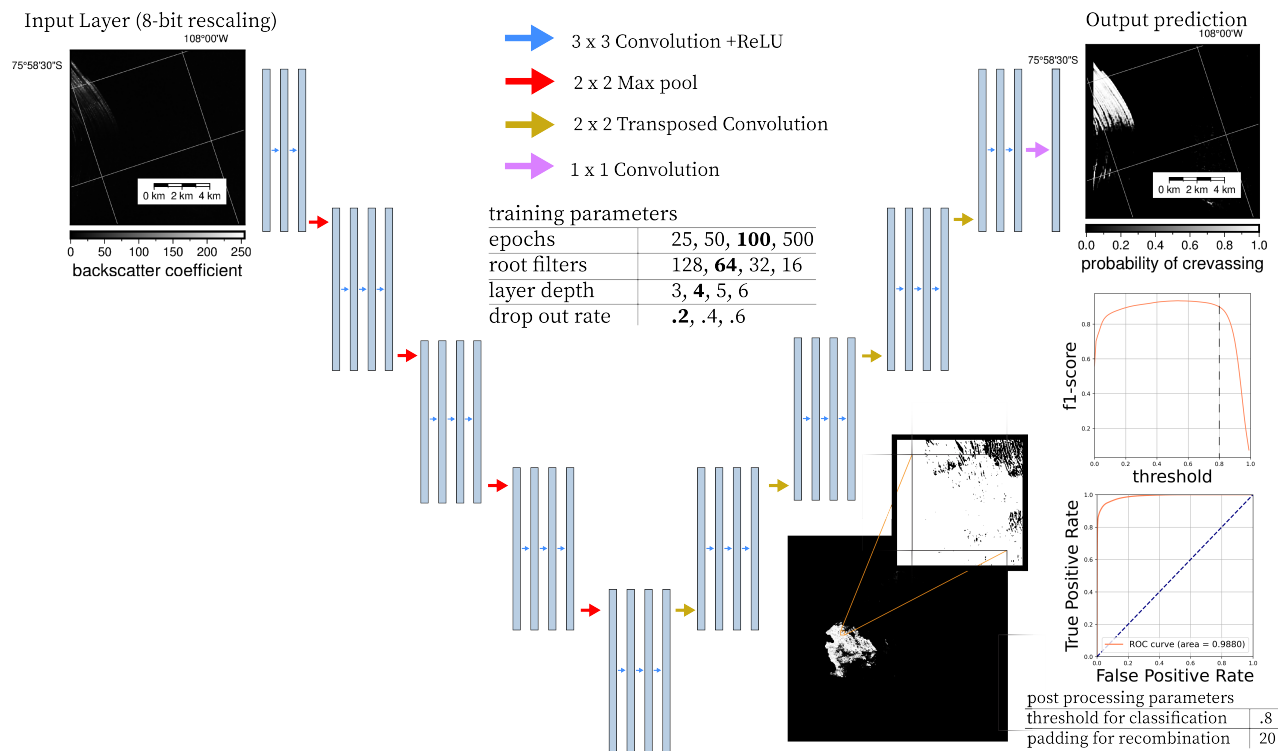
Figure S2. Overview of our implementation of the U-net architecture, the validation results, and the padding scheme used to create the crevasse area time series. The trained newtork produces images with pixel-wise probability of the presence of crevasses. These probabilities are used to create binary detection masks using the F1-score on independent training data. The F1-score is a measure of the accuracy of binary classification algorithms and was used to diagnose the precision and recall of pixel-wise crevasse classification based on a threshold probability.
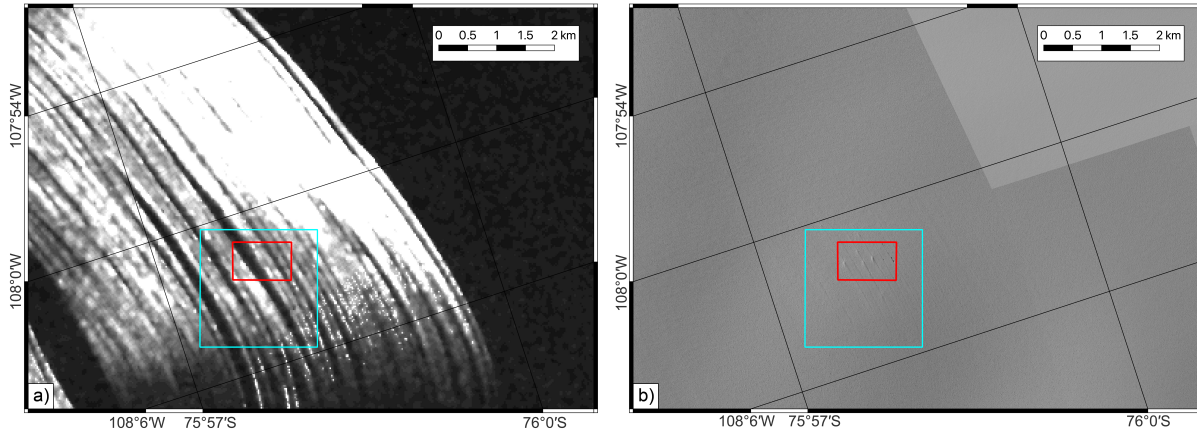
Figure S3. (a) Surface SAR and (b) worldview imagery of lower Thwaites Glacier showing backscatter signals that we use to create maps of surface crevasses with contemporaneous spin drift signals we observe in optical imagery of the partially buried crevasse features.
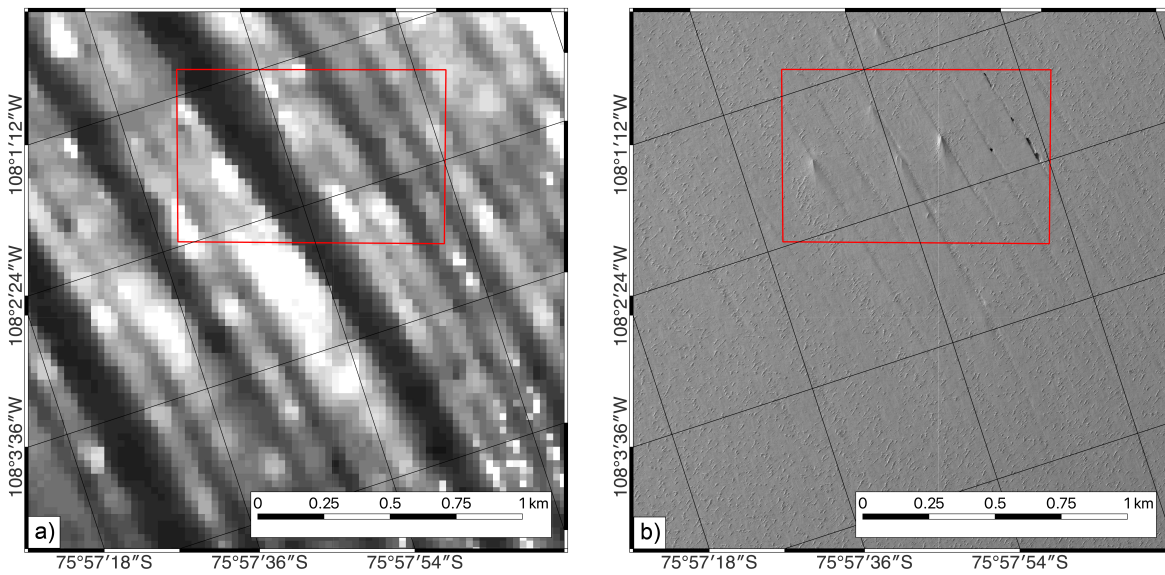

Figure S4. Same crevasse feature as shown in Supplemntary figure S3, but zoomed in to show more detail of optical imagery. (a) Surface SAR and (b) worldview imagery of lower Thwaites Glacier showing backscatter signals that we use to create maps of surface crevasses with contemporaneous spin drift signals we observe in optical imagery of the partially buried crevasse features.
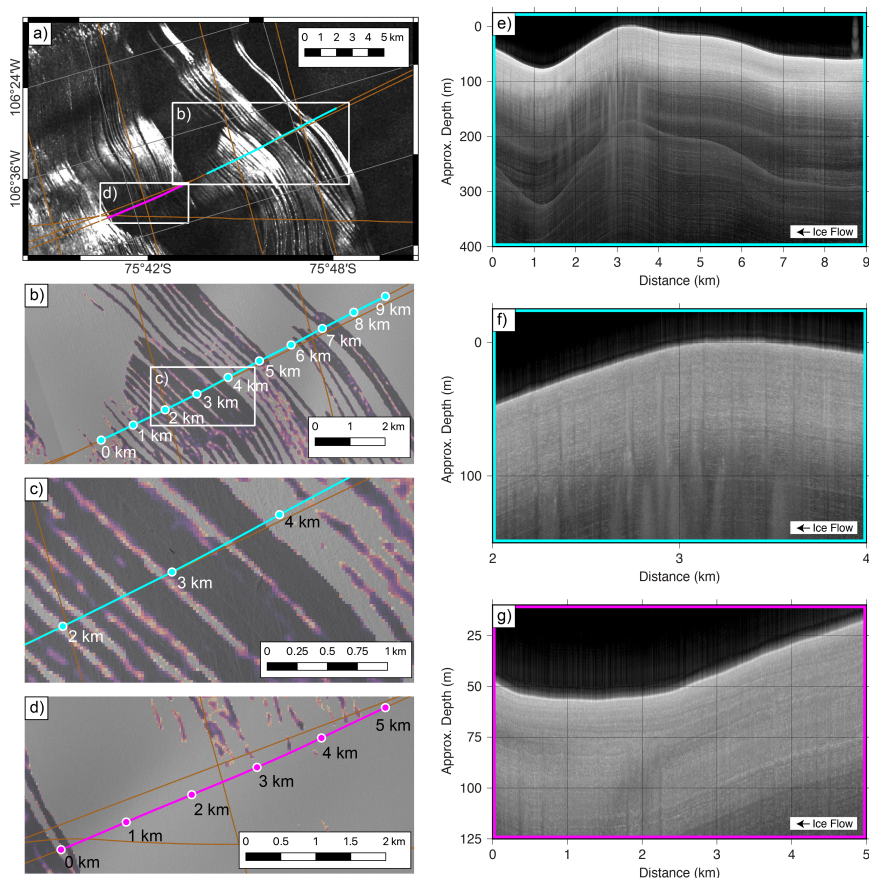
Figure S5. a) Radiometrically corrected reflectivity for a Sentinel-1A synthetic aperture radar image of lower Thwaites Glacier collected on January 28, 2019. Bright quasi-linear features are associated with crevasses. Brown lines mark International Thwaites Glacier Collaboration aerogeophyiscs flight lines collected during the 2018-2019 austral summer with an ultra-wideband (300MHz), ultra-high frequency radar system (750MHz center frequency). Radar profiles shown in this figure were collected on February 1, 2019. Blue (b) and green (d) lines in white boxes mark areas of images highlighted in later panels. b) Panchromatic Worldview image of the white box marked as panel (b) in panel (a). Red colors indicate crevasse prediction likelihood (redder indicates great probability of crevasse). The blue line marks the radar profile shown in panels (e) and (f). Black box marks inset shown in panel (c). Distance along track in the radar profile is noted by black markers with annotation. c) Panchromatic Worldview imagery of inset of panel (c) with same markers and annotation as in the previous panel. These are the only clearly visible crevasses at the surface in Worldview imagery for all insets in this figure. d) Panchromatic Worldview image of the white box marked as panel (d) in panel (a). Red colors indicate crevasse prediction likelihood (redder indicates great probability of crevasse). Green line marks radar profile shown in panel (g). Distance along track in the radar profile is noted by black markers with annotation. e) Accumulation radar profile marked in box (b) in panel (a) and shown in panel (b). Surface crevassing onsets at 1 km along-track distance. Between km 2.26 and 5.5 there are no visible crevasses. Surface and subsurface crevassing is notable again at km 5.5 to the end of the profile. f) A magnified version of the previous panel showing that crevassing is seen near the surface but also deeper (80 m) depth, suggesting burial during advection downstream. g) Accumulation radar profile marked in box (e) in panel (a) and shown in panel (e). Shallow subsurface crevassing starts at 0.3 km along-track distance, but smooth layers are present above crevasses (from the surface to 10-15 m depth). Deeper crevasses are visible in the second half of the profile (50 m depth).
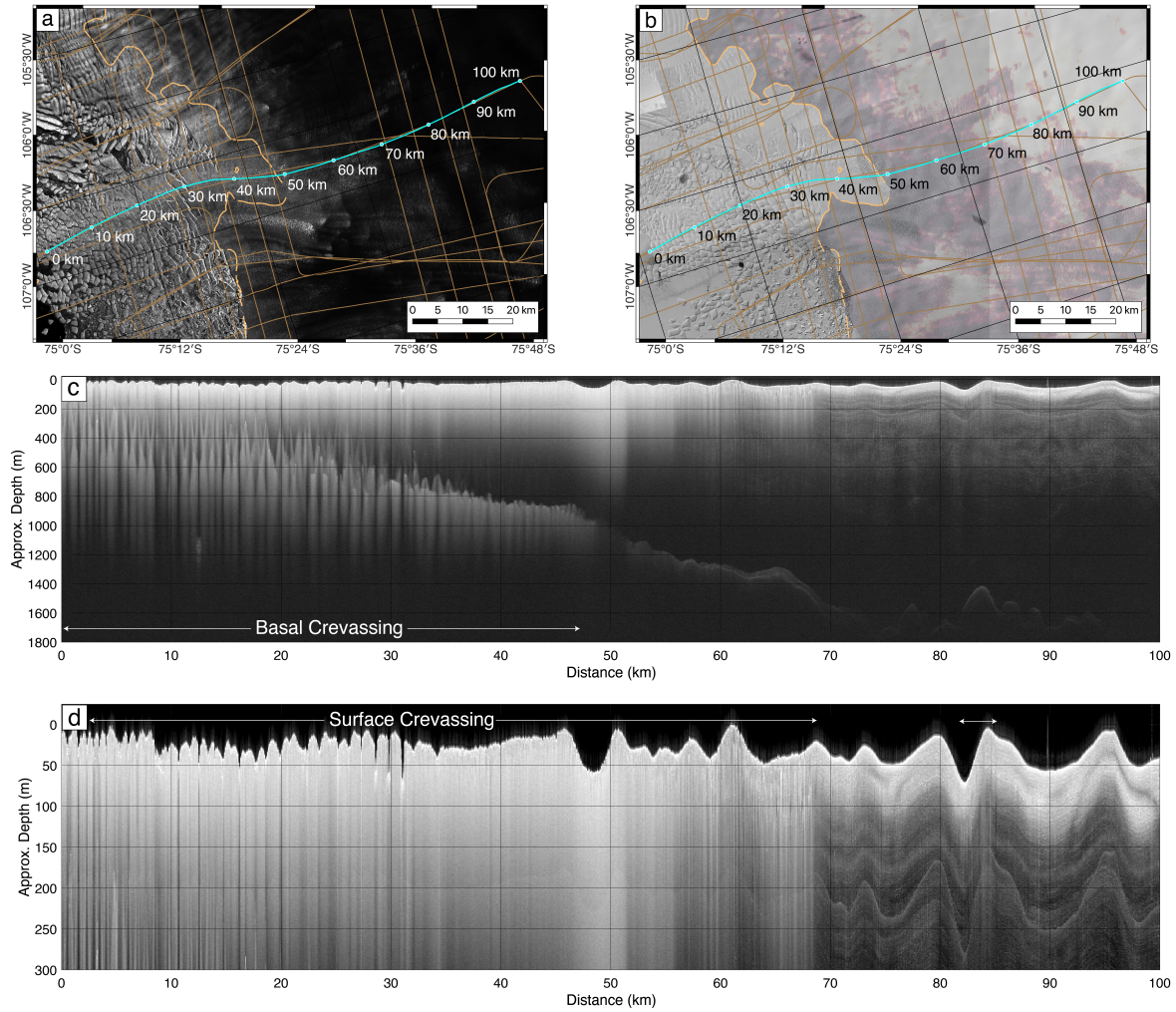
Figure S6. (a-b) Surface SAR and worldview imagery of the Thwaites Ice shelf showing accumulation radar flight lines (brown) with the profiles shown below (blue). (c-d) radargram across the grounded zone. Tips of basal crevasses are identified with black arrows. Also shown are near-surface stratigraphy draped over buried near-surface crevasses that we also image upstream. The density of these near-surface features is visible until the surface slope of the ice sheet increases close to the grounding zone.
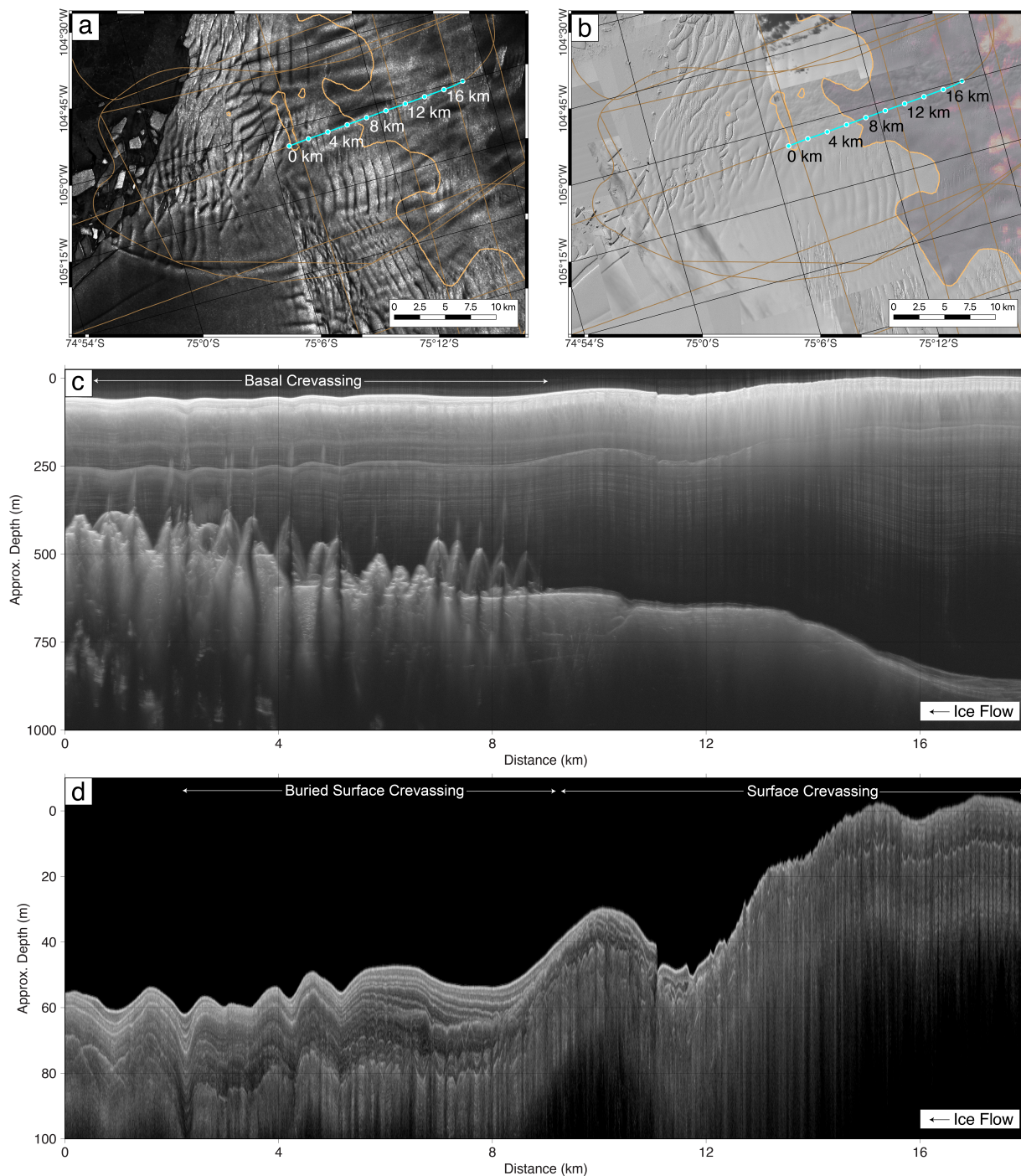
Figure S7. (a-b) Surface SAR and worldview imagery of the Thwaites Ice shelf showing accumulation radar flight lines (brown) with the horizontal positioning of radargram profiles shown in (blue). Below these maps are (c-d) images of the same radargram across the grounded zone. (c) The first radargram shows the full thickness of the ice shelf where black arrows indicate the extent of basal crevasses.(d) The second radargram shows the near surface where snow stratigraphy has buried near surface crevasses.
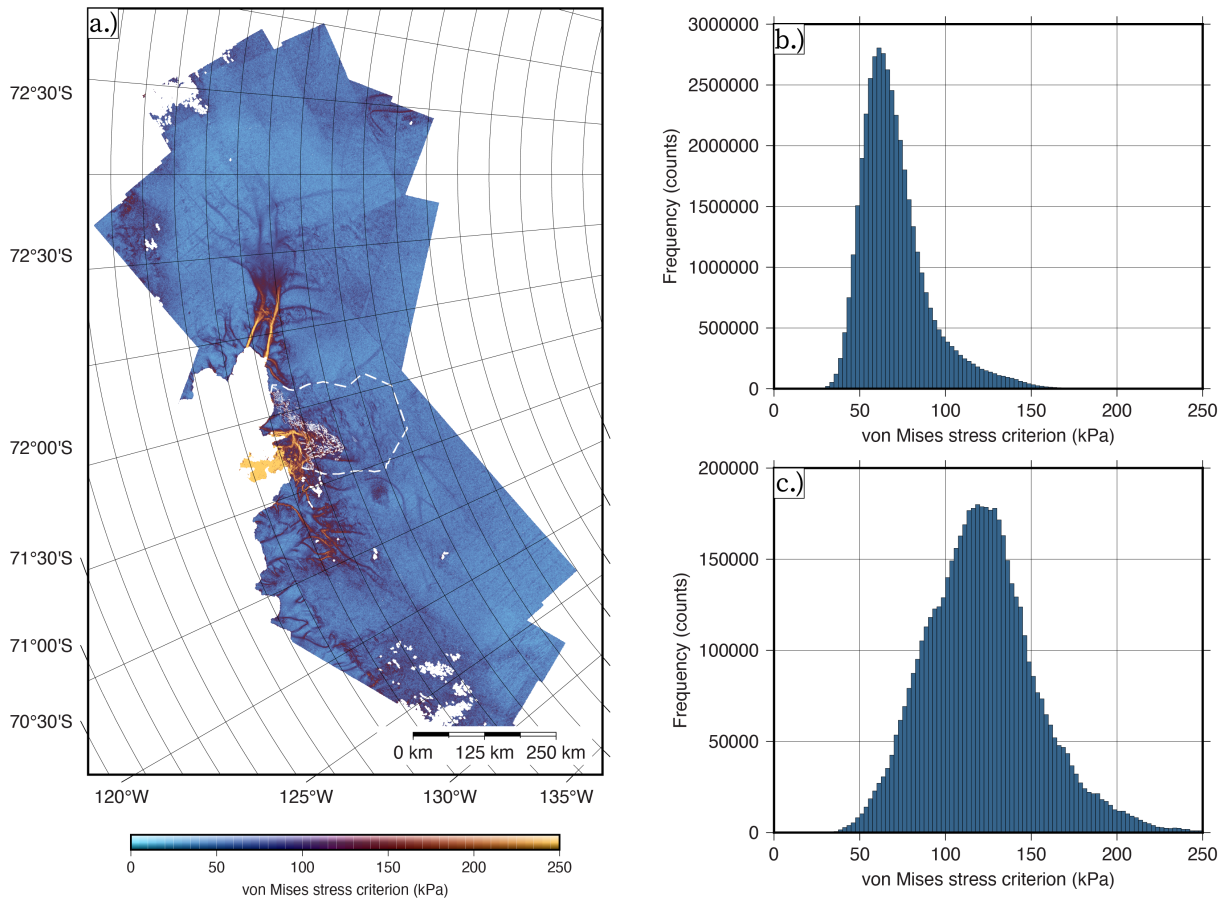
Figure S8. (a) Von Mises Stresses shown with crevasses area (threshold outlined where crevasse probability exceeds .8) for the Amundsen Sea Embayment. Also shown are (b) the histograms of von Mises stresses for uncrevassed regions and (c) crevassed areas for the area outlined in the hashed white line.
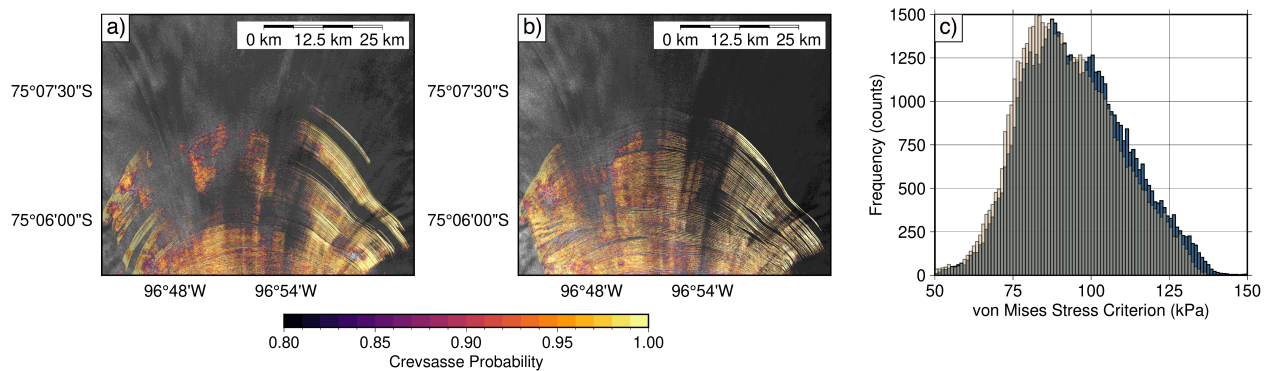
Figure S9. (a) Crevassed area extent using F1-score with crevassed area probability in 2015. (b) Crevassed area extent using F1-score with crevassed area probability using F1-score in 2023. (c) Histogram of change in von mises stress criterion between 2023 and 2015 (2023-2015).

55 References

Alley, K. E., Scambos, T. A., Anderson, R. S., Rajaram, H., Pope, A., and Haran, T. M.: Continent-wide estimates of Antarctic strain rates from Landsat 8-derived velocity grids, Journal of Glaciology, 64, 321–332, https://doi.org/10.1017/jog.2018.23, 2018.

Ambach, W. and Eisner, H.: Proposal for a constitutive equation of temperate firn, Cold Regions Science and Technology, 13, 1–9, https://doi.org/10.1016/0165-232x(86)90002-9, 1986.

60 Ambach, W., Huber, J., Eisner, H., and Schneider, H.: A constitutive equation for temperate firn derived from strain rates of two firn pits (Kesselwandferner, Oetztal Alps, 1967–1989), Cold Regions Science and Technology, 21, 295–303, https://doi.org/10.1016/0165-232x(93)90072-g, 1993.

Ambach, W., Huber, J., Eisner, H., and Schneider, H.: Depth profiles of effective viscosities of temperate firn following from strain rate measurements at two firn pits (Kesselwandferner, Oetztal Alps, 1967–1989), Cold Regions Science and Technology, 23, 257–264,
65 https://doi.org/https://doi.org/10.1016/0165-232X(94)00017-R, 1995.

Arthern, R. J., Vaughan, D. G., Rankin, A. M., Mulvaney, R., and Thomas, E. R.: In situ measurements of Antarctic snow compaction compared with predictions of models, Journal of Geophysical Research: Earth Surface, 115, F03 011, https://doi.org/10.1029/2009jf001306, 2010.

Bindschadler, R., Vornberger, P., Blankenship, D., Scambos, T., and Jacobel, R.: Surface velocity and mass balance of Ice Streams D and E,
70 West Antarctica, Journal of Glaciology, 42, 461–475, https://doi.org/10.3189/s0022143000003452, 1996.

Cuffey, K. M. and Paterson, W. S. B.: The Physics of Glaciers Fourth Edition, 2010.

Grinsted, A., Rathmann, N. M., Mottram, R., Solgaard, A. M., Mathiesen, J., and Hvidberg, C. S.: Failure strength of glacier ice inferred from Greenland crevasses, EGUsphere, 2023, 1–15, https://doi.org/10.5194/egusphere-2023-1957, 2023.

Haefeli, R.: Some Results of the International Glaciological Expedition to Greenland 1957-1960: Concerning the Rheological Behaviour of
75 Snow and Ice, in: Physics of Snow and Ice: proceedings, vol. 1 of *2*, pp. 983–991, 1967.

Lai, C.-Y., Kingslake, J., Wearing, M. G., Chen, P.-H. C., Gentine, P., Li, H., Spergel, J. J., and van Wessem, J. M.: Vulnerability of Antarctica's ice shelves to meltwater-driven fracture, Nature, 584, 574–578, https://doi.org/10.1038/s41586-020-2627-8, 2020.

Morris, E. M. and Wingham, D. J.: Densification of polar snow: Measurements, modeling, and implications for altimetry, Journal of Geophysical Research: Earth Surface, 119, 349–365, https://doi.org/10.1002/2013jf002898, 2014.

80 Nye, J. F.: A Method of Determining the Strain-Rate Tensor at the Surface of a Glacier, Journal of Glaciology, 3, 409–419, https://doi.org/10.3189/s0022143000017093, 1959.

Vaughan, D. G.: Relating the occurrence of crevasses to surface strain rates, Journal of Glaciology, 39, 255–266, https://doi.org/10.3189/s0022143000015926, 1993.

Veen, C. J. v. d.: Crevasses on glaciers, Polar Geography, 23, 213–245, https://doi.org/10.1080/10889379909377677, 1999.